Recent Progress on Microwave Imaging Technology and New Physics Results*)

Benjamin TOBIAS[1,2)], Neville C. LUHMANN, Jr.[1)], Calvin W. DOMIER[1)], Xiangyu KONG[1)], Tianran LIANG[1)], Shao CHE[1)], Raffi NAZIKIAN[2)], Luo CHEN[3)], Gunsu YUN[4)], Woochang LEE[4)], Hyeon K. PARK[4)], Ivo G.J. CLASSEN[5)], Jurrian E. BOOM[5)], Anthony J.H. DONNÉ[5,6)], Michael A. Van ZEELAND[7)], Réjean BOIVIN[7)], Yoshio NAGAYAMA[8)], Tomokazu YOSHINAGA[8)], Daisuke KUWAHARA[9)], Soichiro YAMAGUCHI[10)], Yuichiro KOGI[11)], Atsushi MASE[12)] and Tobin L. MUNSAT[13)]

[1)] *University of California at Davis, Davis, CA 95616*
[2)] *Princeton Plasma Physics Laboratory, Princeton, NJ 08543*
[3)] *University of Science and Technology of China, Hefei, China*
[4)] *POSTECH, Pohang, Gyeongbuk 790-784, Korea*
[5)] *FOM-Institute for Plasma Physics Rijnhuizen, 3430 BE Nieuwegein, The Netherlands*
[6)] *Eindhoven University of Technology, 5600 MB Eindhoven, The Netherlands*
[7)] *General Atomics, San Diego, CA 92121*
[8)] *National Institute for Fusion Science, Toki, Gifu 509-5252, Japan*
[9)] *Tokyo Institute of Technology, Tokyo, Japan*
[10)] *Kansai University, Osaka, Japan*
[11)] *Fukuoka Institute of Technology, Fukuoka 811-0295, Japan*
[12)] *Kyushu University, Fukuoka 812-8581, Japan*
[13)] *University of Colorado, Boulder, CO 80309*

(Received 26 January 2011 / Accepted 17 February 2011)

Techniques for visualizing turbulent flow in nature and in the laboratory have evolved over half a millennium from Leonardo da Vinci's sketches of cascading waterfalls to the advanced imaging technologies which are now pervasive in our daily lives. Advancements in millimeter wave imaging have served to usher in a new era in plasma diagnostics, characterized by ever improving 2D, and even 3D, images of complex phenomena in tokamak and stellarator plasmas. Examples at the forefront of this revolution are electron cyclotron emission imaging (ECEI) and microwave imaging reflectometry (MIR). ECEI has proved to be a powerful tool as it has provided immediate physics results following successful diagnostic installations on TEXTOR, ASDEX-U, DIII-D, and KSTAR. Recent results from the MIR system on LHD are demonstrating that this technique has the potential for comparable impact in the diagnosis of electron density fluctuations. This has motivated a recent resurgence in MIR research and development, building on a prototype system demonstrated on TEXTOR, toward the realization of combined ECEI/MIR systems on DIII-D and KSTAR for simultaneous imaging of electron temperature and density fluctuations. The systems discussed raise the standard for fusion plasma diagnostics and present a powerful new capability for the validation of theoretical models and numerical simulations.

Keywords: plasma diagnostics, millimeter-wave imaging, electron cyclotron emission, reflectometry, electron temperature fluctuation, electron density fluctuation

DOI: 10.1585/pfr.6.2106042

1. Introduction

Advancements in millimeter-wave technology and improved diagnosis of electron temperature and density behavior in fusion plasmas have gone hand in hand since proof-of-principle ECEI and MIR prototype systems were realized on the TEXTOR tokamak in [1, 2]. In the case of ECEI, the spontaneous emission of black-body radiation from the optically thick second harmonic X-mode occurs at $2f_{ce} \cong 56 \times B\,\mathrm{GHz}$, where B is the magnetic field in Tesla. MIR makes use of reflection at the right hand plasma cutoff, $f_R = \left[f_{ce} + \left(f_{ce}^2 + 4f_{pe}^2\right)^{1/2}\right]/4\pi$, where $f_{pe} \cong 9\sqrt{n_e}\,\mathrm{Hz}$ and n_e is the electron density in m^{-3}, to couple transmitter and receiver sections of a millimeter-wave radar system. Therefore, the development of diagnostic techniques has hinged on advancements in quasi-optical filtering and coupling of millimeter waves in heterodyne

author's e-mail: ncluhmann@ucdavis.edu

*) This review article is based on the presentation at the 20th International Toki Conference (ITC20).

detection systems.

By incorporating planar frequency selective surfaces and sophisticated imaging antenna array configurations, ECEI has attained the status of a mature diagnostic technique capable of providing unique opportunities for experimental validation of theoretical models [3]. Dual-array ECEI systems at DIII-D [4] and KSTAR [5] represent the state of the art in this technique. New physics results from these machines illustrate the potential of these new data for unambiguous observation of key features which distinguish competing descriptions and theoretical models of long studied instabilities such as the sawtooth oscillation [6–8] and Alfvén eigenmodes [9, 10].

Both ECEI and MIR are extensions of 1D diagnostic techniques which have been widely employed for several decades. The application of imaging techniques to reflectometry has the added benefit of collecting scattered radiation at a wide range of angles, thereby improving the integrity of the measurement made by any single detector [11]. Imaging multiple detectors to multiple cutoff surfaces to produce a 3D image of electron density fluctuations has been accomplished on LHD. The LHD MIR design meets the significant challenge of coupling illumination and receiver systems with a sophisticated arrangement of adjustable reflective optics and an advanced horn-antenna mixer array (HMA).

Building upon the successes of LHD MIR with new systems at DIII-D and KSTAR requires a careful design process which makes use of lessons learned over a decade of advancements in quasi-optical antenna coupling in the presence of turbulent fluctuations. A prototype TEXTOR MIR system facilitated the identification of critical areas which have demanded further improvement [12]. Improved modeling of the plasma wave interaction [13], coupled with quasi-optical imaging design techniques refined throughout the development of ECEI systems, result in a synthetic diagnostic capable of addressing these outstanding questions [14, 15].

2. DIII-D and KSTAR ECEI Systems

The simplest analogy which describes ECEI is that of a millimeter wave video camera capturing electron temperature fluctuations in real time. Each ECEI array, with up to 24 vertical channels and 8 radial channels separated in frequency, provides a 2D picture of a variable portion of the poloidal plane [3]. Both the DIII-D and KSTAR ECEI systems are dual-array configurations providing images at two distinct plasma locations. The images may be independently configured to capture adjacent regions or opposing sides of the magnetic axis. Additionally, the vertical and radial coverage of each image may be varied over a broad range. Switching of RF channel spacing allows for a 1.5:1 radial zoom factor. Vertical zoom is accomplished by large aperture plasma coupling optics with a continuous range of adjustment.

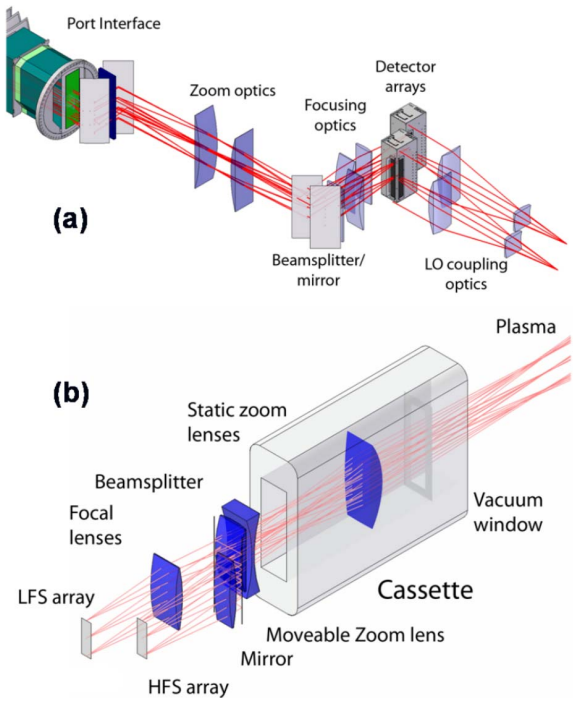

Fig. 1 Dual array ECEI systems at DIII-D (a) and KSTAR (b) are shown. On DIII-D (a), vertical zoom functionality is provided by a translating lens doublet which couples both high and low field side detector arrays. On KSTAR (b), a triplet zoom lens is housed in a cassette inside the tokamak cryostat, allowing for placement very near the plasma for exceptional vertical coverage. *Adapted from Ref.* [16].

DIII-D and KSTAR are similarly sized tokamaks operated with comparable magnetic field configurations during the 2010 experimental campaign. However, the access constraints on these machines are very different, leading to very different solutions to the challenges of optical coupling [16]. In each case, a thin film dielectric beamsplitter is used to combine separate arrays and objective lens systems optimized for operation at the low and high field sides of the plasma, respectively. A zoom lens is incorporated into the vacuum interface and shared by both sub-systems. While every effort has been made to standardize all other major sub-systems in modern ECEI diagnostics, the design of the vertical zoom lens sub-system is very different on DIII-D and KSTAR. Figure 1 presents these designs side by side for comparison.

The vertical zoom lens design on DIII-D is optimized with consideration for constraints posed by a vacuum interface which is mechanically robust and places the fused silica glass window at an angle which minimizes thermal stress, erosion, and material deposition for exceptional transmission characteristics under harsh conditions and over a long service lifetime. These benefits are at the cost of proximity to the plasma, and the first lens element may be placed no closer than 1.5 m to the plasma edge. A doublet zoom lens allows the diagnostic to image a total vertical span of up to 60 cm with 20 vertical channels.

The lens design is mechanically compensated, requiring that both lenses move independently [3].

In contrast, a specially designed zoom optics cassette allows the vacuum window, and hence the zoom optics, to be placed inside the cryostat and near the plasma edge on KSTAR. The result is that a triplet zoom lens design may be used, maximizing the vertical coverage. This optically compensated design requires translation of only the central, negative element, and images up to 1 m vertically with 24 channels [5]. A parabolization of the final plasma facing surface ensures that this 3:1 magnification of the detector array does not result in significant aberration at the image plane.

The efficient design of sophisticated optical coupling systems such as those described above is made possible by recent improvements in imaging detector arrays. Figure 2 shows a standard ECEI detector array as used on both DIII-D and KSTAR. Dual dipole antennas, optimized for wideband detection over multiple waveguide frequency bands (in this case W and F band, spanning 75 to 140 GHz), are coupled to individual elliptical substrate mini-lenses [17, 18]. This arrangement results in a high gain, Gaussian antenna pattern for each element. The use of multiple individual mini-lenses simplifies the description of the array for the purposes of coupling signal and LO power. RF and LO power are injected at opposing ports of the detector array. A 3 dB beamsplitter combines RF and LO power at two sub-arrays of detectors which are offset vertically but imaged to the same plasma region. The top view of this arrangement in shown in Fig. 2 (a), while the mini-lenses themselves are visible through the open RF ports in Fig. 2 (b). This technique allows imaged plasma volumes to be packed more densely than the physical spacing of the mini-lenses and eliminates the need for a beam dump, improving LO efficiency.

Figure 2 (c) shows the banks of 2-18 GHz low noise IF amplifiers which provide greater than 20 dB of gain for signals produced at the first heterodyne downconversion step. The second downconversion step is performed by a complement of IF/detector modules which may be remotely located away from the noisy environment of the experimental hall. The frequencies of the eight voltage controlled oscillator (VCOs) used in the final downconversion step determine the radial spacing of the sample volumes, while low-pass filtering of the resulting double sideband RF response determines the radial sample volume, or radial resolution [19]. A compromise between resolution and the background thermal fluctuation noise level is made in selecting a fixed channel RF bandwidth of 700 MHz ($\sim$ 1.5 cm radial resolution). The spacing of these channels is switchable, however, from 600 to 900 MHz, resulting in a radial zoom capability.

At the forefront of ECEI diagnostic development is the ongoing design of new IF/detector modules which will utilize the entire 2-18 GHz IF signal available from the detector arrays to produce 16 radial channels (i.e., double the current number). A block diagram of the strategy used is shown in Fig. 3. Recent improvements to commercially available voltage controlled oscillators (VCOs) allow for off the shelf components to be employed up to 15.5 GHz. The highest local oscillator frequency of 16.4 GHz will be provided by a surface mount frequency doubler. The 16 radial channels of the upgraded diagnostic will make full use of the currently available IF bandwidth; further improvements are planned through a redesign of the detector array and expansion of the bandwidth of key components, such as baluns and IF amplifiers.

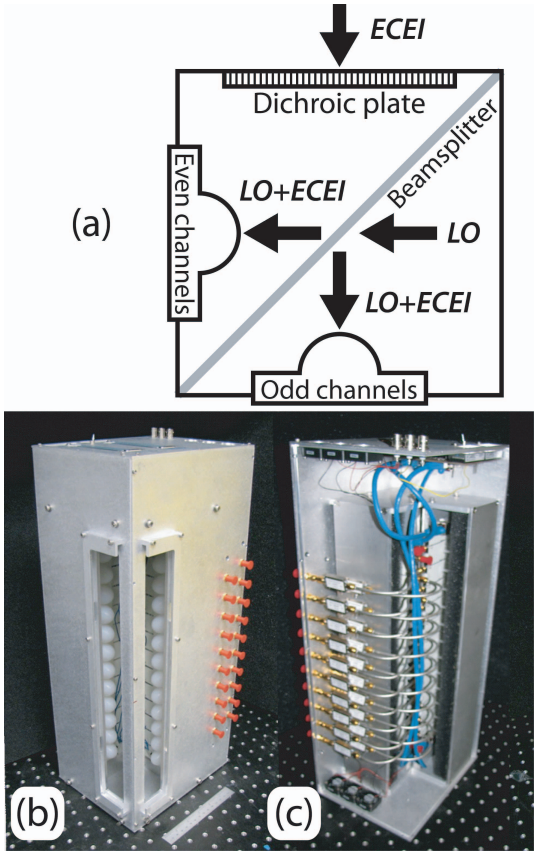

Fig. 2 (a) An illustration of the RF and LO coupling arrangement as seen from above. Detector sub-arrays are placed at the transmitted and reflected sides of both paths, eliminating the need for a beam dump. (b) The open RF ports of the standardized detector array reveal the miniature substrate lenses. During operation, dichroic plates cover these ports and provide both lower sideband rejection and electromagnetic shielding. (c) Low noise IF amplifiers are housed inside the rear compartment of the detector array completing a ruggedized stand-alone unit which may be remotely located from more delicate signal processing electronics. *Reprinted with permission from Ref.* [16].

3. Recent Physics Results from ECEI

The power of ECEI data is best demonstrated by its ability to provide immediate physics results. With each improvement in the diagnostic technique come new obser-

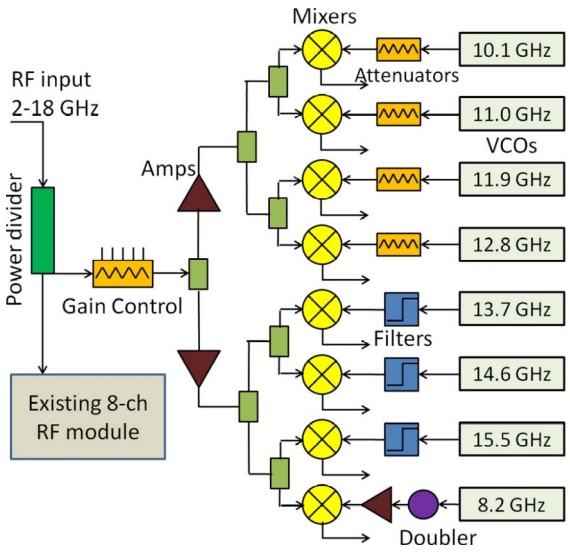

Fig. 3 A block diagram of the RF circuit which will extend ECEI systems to image 16 radial channels, making use of the full 2-18 GHz IF bandwidth provided by the current imaging array design. For frequencies above 12.8 GHz, a low pass filter is added to remove sub-harmonic local oscillator frequencies which may interfere with lower frequency channels. Solid state VCOs are commercially available up to 15.5 GHz, while a surface mount frequency doubler IC will provide the highest frequency LO at 16.4 GHz.

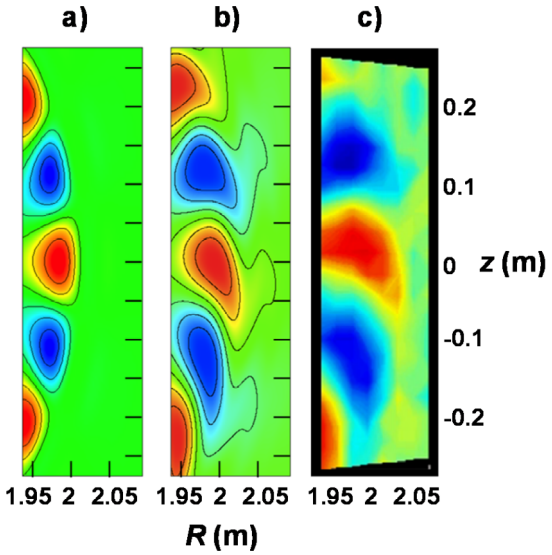

Fig. 4 A reversed shear induced Alfvén eigenmode (RSAE) observed on DIII-D is compared to modeling in numerical eigenmode solvers. (a) In an ideal-MHD approximation, the $n = 4$ RSAE is predicted at 65 kHz for the experimentally obtained thermal plasma equilibrium. (b) A non-perturbative hybrid gyrofluid-MHD model implemented by TAEFL reproduces the same mode, but includes a distortion also observed by ECEI (c). *Adapted from Ref.* [20].

vations. The state of the art imaging properties of the DIII-D ECEI system have provided the resolution necessary to identify, unambiguously, subtle features which challenge the predictive capability of present day MHD eigenmode solvers. In particular, symmetry breaking in Alfvén eigenmodes such as that shown in Fig. 4 reveals the pervasiveness of non-perturbative effects [10].

The phase distortion shown in Fig. 4 is precluded by symmetry constraints imposed in the ideal-MHD approximation adopted by eigenmode solvers such as NOVA [21]. While a phase ramp along the tokamak midplane has been previously reported [22], 2D measurement removes ambiguity and associates this feature with poloidal distortion of the mode. These distortions may be compared directly to non-perturbative eigenmode solvers such as TAEFL [22], resulting in new opportunities for model validation. New avenues of exploration are now available which will lead to greater predictive capability for future regimes employing off-axis NBI plasma heating and current drive, as well as in burning plasmas where it is fusion alpha particles which have the greatest likelihood of exciting Alfvén modes.

An exciting new area of application for ECEI is in characterizing plasma behavior in the edge and pedestal regions, including regions where the plasma is optically thin or grey. Sufficient cyclotron radiation is emitted from these regions to realize favorable signal to noise ratios. However, the plasma no longer emits as a black body, and therefore interpretation of the emission is challenging. Localization of the emission volume suffers from spreading of the resonance, reflection from vessel surfaces, and in some cases shine-through from overlapping harmonics at the high field side. Furthermore, the radiation temperature is no longer a linear function of electron temperature, but additionally has a strong dependence on electron density.

In the diagnosis of plasma fluctuations such as those relevant to the geodesic acoustic mode (GAM) [23, 24], the density dependence of the radiation temperature may be beneficially dominant. When the plasma is optically thin and it is assumed that $\tilde{n}_e/\langle n_e\rangle \gg 2\tilde{T}_e/\langle T_e\rangle$, then the fluctuating temperature $\tilde{T}_*$ observed by the radiometer is described by [5],

$$\frac{\tilde{T}_*}{\langle T_*\rangle} = 2\frac{\tilde{T}_e}{\langle T_e\rangle} + \frac{\tilde{n}_e}{n_e}. \quad (1)$$

Here, bracketed quantities represent time averages. It is clear from this expression that, particularly in cases where steep density gradients in the pedestal region provide a cut-off surface which prevents additional contributions from overlapping harmonics and internal wall reflection, fluctuation in radiometer signal may be interpreted as density fluctuation.

Imaging of edge localized modes (ELMs) on ASDEX-U [9] has shown that ECEI provides interesting data which, with careful interpretation, lends insight into the dynamic behavior of these modes. In Fig. 5, ECEI images from before and after an ELM crash are shown. Preceding the crash, the plasma region near the separatrix is dominated

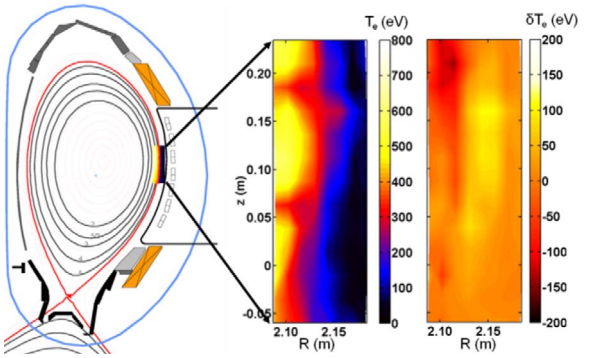

Fig. 5 ECEI data showing edge activity (a) before and (b) after an ELM crash. The ELM is preceded by fluctuations with high toroidal mode number in a region of steep density and temperature gradients. After the ELM crash, filamentary structures are observed outside the separatrix. *Adapted from Ref.* [9].

by high toroidal mode numbers which produce long wavelength coherent turbulence. After the ELM crash, however, the turbulence has subsided. A hot filament structure is seen propagating poloidally outside the separatrix. Absolute determination of the density and temperature of this filament is difficult as the optical thickness at the separatrix is estimated to be unity. However, the 2D nature of ECEI identifies poloidal localization of the emission and a finite bandwidth, if not radial localization.

An opportunity exists for answering some questions about the utility of ECEI as a diagnostic for plasma edge measurements in the form of upgrades to the DIII-D ECEI system which will be fully implemented during the 2011 experimental campaign. The use of zero biased detectors in upgraded IF electronics modules will greatly improve the stability of the diagnostic offset value, which in previous experiments was shown to drift several mV during the course of a single discharge. Removing this drift allows ECEI to measure slow fluctuations associated with evolution of the plasma profile with greater accuracy. Additionally, quantitative images of slowly rotating ($\sim$ 10-50 Hz) resonant magnetic perturbations (RMPs) will now be available.

Comparison of ECEI data to these known fluctuations, with the aid of enhanced Thomson scattering capabilities at DIII-D, will allow for the questions raised above to be addressed in a focused and well-motivated manner. With a method for confidently interpreting ECEI measurements in the edge and pedestal regions, a wide variety of applications will arise, including characterization of novel ELM control methods, advanced operating and startup scenarios, and a broad range of 3D field effects.

4. Recent Advancements in MIR

Microwave imaging reflectometry (MIR), like ECEI, makes use of a broad range of technical advancements in

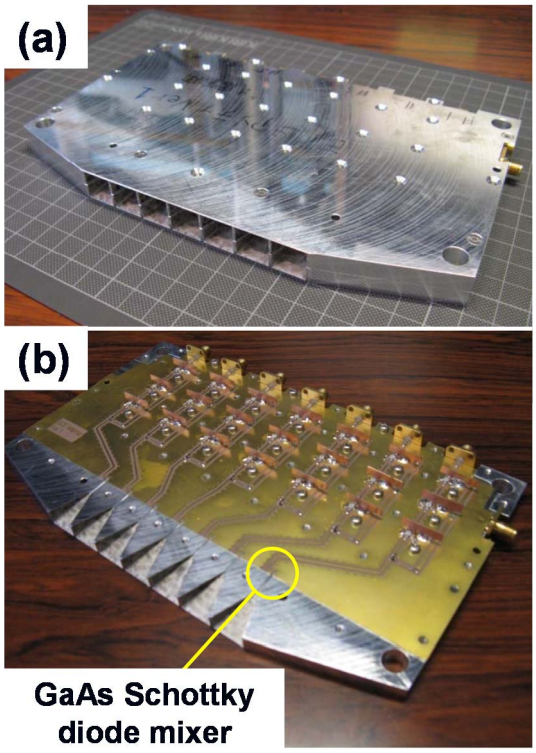

Fig. 6 The LHD MIR horn mixer array (HMA). (a) The assembled 7 channel unit comprises a stackable, shielded 1D array which may be fed with multiple frequencies over the 50-110 GHz operating range of the GaAs Schottky diode mixer. Removing the cover as in (b) reveals the enclosed mixing element and three stage IF amplification on an integrated printed circuit board (PCB). LHD MIR utilizes 5 of the units shown with 4 illumination frequencies for a total of 140 reflectometer channels.

order to achieve a 2D, or even 3D, extension of a 1D diagnostic technique. With multiple detectors and multiple operating frequencies, MIR promises to provide a capability for diagnosis of spatially localized density fluctuations comparable to that realized by ECEI for temperature fluctuations. The MIR system on LHD [25–27] represents a groundbreaking achievement in 3D imaging of density fluctuations, and provides data key to understanding the transport properties of this stellarator device.

At the heart of the LHD MIR system is a horn mixer array (HMA) which combines well-characterized pyramidial horn antennas, Schottky diode mixers, and IF amplification in a single shielded and expandable unit. As shown in Fig. 6, a linear array of 7 waveguide horns is packaged together with the first stage RF circuitry. These 7 channel arrays may be combined in an arbitrarily large stack, providing a 2D arrangement of detectors. The LHD MIR system is composed of 5 such arrays for a total of 35 antennas (5 toroidal by 7 poloidal). These are each driven by 4 illumination sources (60.41, 61.81, 63.01, and 64.61 GHz) and a single LO mixing frequency of 55.8 GHz. The result is a 140 channel 3D volume of imaged density fluctuations.

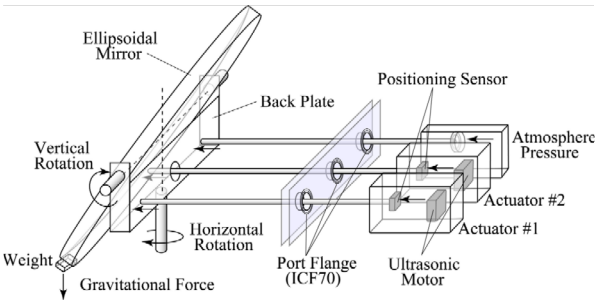

Fig. 7 Adjustment of the main mirror for the LHD MIR system is performed by two ultrasonic actuators. Vertical adjustment is balanced by the weight of the mirror, while horizontal adjustment is balanced by atmospheric pressure. Position sensors at the motorized actuators provide constant feedback control.

The complicated 3D shape of cutoff surfaces in LHD requires careful alignment and focusing of both transmit and receive elements. This is performed by the steerable in-vacuum mirror illustrated in Fig. 7. An ultrasonic motor allows for fast adjustment and control of vertical and horizontal positioning. This is particularly important as it has been observed that the optimum region of adjustment is less than 1 degree.

It may be demonstrated analytically that sinusoidal phase modulation of the reflectometer probe beam by a phase screen results in the generation of sidebands of symmetric diffraction orders [28]. Allowed to propagate freely to the detector plane, these sidebands result in a perturbation of the diffracted field which rotates in the complex plane as a function of propagation distance. The result is an additional contribution to either phase or amplitude of the reflectometer signal. For small fluctuations, this contribution may be detected in the phase of sideband correlations. Numerical techniques have been proposed which use this information to perform a synthetic back projection of reflectometer data, thereby extracting the maximum phase information from the reflectometer signal and removing the unwanted amplitude distortions [29]. The procedure is analogous to optical imaging, however, and suggests that a well designed imaging diagnostic may solve this problem for a wide variety of experimental conditions and unknown fluctuation parameters. This is the true advantage of MIR, and is the subject of intensive investigation.

Key to the generation of symmetric diffraction sidebands is uniform and perpendicular illumination of the phase screen. In the toroidal geometry of a tokamak, this corresponds to curvature matching between phase fronts of the illumination beam and the virtual plasma cutoff surface, which differs from the actual cutoff surface due to refractive effects [11, 30]. Laboratory characterizations of the proof-of-principle TEXTOR MIR system undertaken at POSTECH reveal that this condition could not have been achieved for all operating scenarios [12]. Rather, flaws in both illumination and receive optics which limited the performance of this diagnostic were identified. Many of these flaws may now be corrected by application of design techniques developed for ECEI. However, because the TEXTOR MIR diagnostic performed well in many cases, construction of MIR systems at KSTAR and DIII-D is preceded by a detailed investigation of fundamental principles of reflectometry and candidate diagnostic systems using a variety of numerical simulations and synthetic diagnostics.

A primary consideration for performance is the size of optical apertures. Diffraction of the reflected beam produces significant spreading, particularly for strong fluctuations. Estimations of this spreading may be obtained for the case of reflection from a sinusoidal phase screen. In light of the available port access on KSTAR, it is estimated that the probed fluctuations are constrained approximately as $\lambda_\theta \lambda_0 / a \geq 10\,\mathrm{cm}$, where λ_θ is the fluctuation wavelength, λ_0 is the illumination wavelength, and a is the peak to peak amplitude of the corrugation [31]. At greater fluctuation amplitude or wavenumber, a significant portion of the reflected signal is not collected by the receive optics. Under these conditions, the efficacy of MIR is uncertain and performance should be evaluated by synthetic diagnostics.

A synthetic diagnostic for the sophisticated optical arrangements proposed for future MIR systems requires two separate components: a code for evaluating the performance of the optical system in vacuum, including imperfections of the optical system such as misalignments and spherical aberrations, and a separate code for evaluating the complicated plasma wave interaction in the presence of turbulence. Separation of these components allows a broad survey of candidate optical arrangements to be refined and tested without a need to duplicate time consuming plasma simulations. A coupling of these codes is simplified by applying principles of reciprocity for transmit and receive components of the candidate designs and treating the problem as one of antenna coupling. Input and output fields are coupled by simple integration as in the well known Friis transmission equation. A block diagram of this scheme is presented in Fig. 8, where one of several commercially available optical codes, CodeV, is chosen to simulate the lens system.

Reflection from a thin phase screen, such as a corrugated mirror, may be evaluated by a full wave solution of Maxwell's equations. For modest fluctuation wavelength and amplitude, it has been shown that more efficient analytical approaches, such as a Bessel function expansion of the reflected fields [30] or the use of geometric optics [28], are adequate. Unfortunately, the limits at which these approximations break down are nearly the same as those at which the performance of reflectometer systems falters. Efficient, yet powerful, 2D and 3D reflectometer codes which make use of full wave FDTD analysis near the plasma cutoff and paraxial wave propagation in plasma regions of low refraction are available and allow for an accurate representation of the plasma wave interaction for short fluctuation wave-

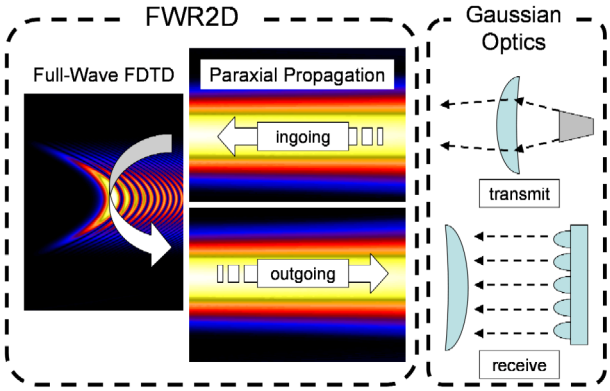

Fig. 8 A block diagram of a synthetic diagnostic technique for the evaluation of candidate MIR designs. An illumination beam is introduced into FWR2D [13]. The incoming beam is propagated by the paraxial Helmholtz equation toward the plasma cutoff. Near the cutoff layer, a full wave solution of the plasma wave interaction is obtained. After propagating paraxially to the plasma edge, the resulting field is convolved with the antenna pattern of the receive optics, which is by reciprocity equivalent to the receiver field of view.

length and large fluctuation amplitude [13]. It remains to be seen whether or not an optimization of MIR may provide a robust solution to the challenging task of quantitatively diagnosing these types of turbulence.

5. Conclusion and Outlook

There is broad ranging motivation for simultaneous diagnosis of density and temperature fluctuations. In the study of anomalous transport due to turbulence, phase relationships between density and potential fluctuations govern energy flux. For electrostatic electron turbulence, such as electron temperature gradient (ETG) and ion temperature gradient (ITG) modes, the anomalous electron energy flux may be expressed as [32],

$$Q_e = \frac{3}{2}\frac{nk_B T_e}{B_t}\left[\left\langle\left(\tilde{T}_e/T_e\right)\tilde{E}_\perp\right\rangle + \left\langle\left(\tilde{n}_e/n_e\right)\tilde{E}_\perp\right\rangle\right]. \quad (2)$$

Interestingly, the above expression implies that anomalous transport is determined not only by plasma fluctuation phase relative to the fluctuating perpendicular electric field, $\tilde{E}_\perp$, a quantity which is challenging to diagnose, particularly in the plasma core, but also by the relative phase of fluctuating electron temperature, $\tilde{T}_e$, and density, $\tilde{n}_e$. This cross-phase has been applied as a constraint for validation of gyrokinetic simulations [33,34] by comparing the phase of temperature fluctuations observed by correlation electron cyclotron emission (CECE) to both beam emission spectroscopy (BES) [35] and reflectometer data [36]. The 2D nature of ECEI and MIR provides an extended variety of correlation lengths and image configurations, including off-axis diagnostic capabilities. This advancement in diagnostic capability becomes increasingly important as the influence of plasma shape on anomalous transport is explored.

In addition to the effects of broadband turbulence, the understanding of coherent modes is also enhanced by simultaneous measurement of density fluctuations. Temperature perturbations observed by ECEI are related to plasma displacement, ξ, by [37],

$$\frac{\delta T_e}{\langle T_e\rangle} = -\xi\cdot\frac{\nabla\langle T_e\rangle}{\langle T_e\rangle} - (\gamma-1)\nabla\cdot\xi, \quad (3)$$

where γ is the adiabatic index. For slow fluctuations, the compressional term at the right may be ignored as, according to kinetic theory, the electron population is thermalized along a magnetic field line, i.e. $\gamma \to 1$. However, for oscillations with frequencies comparable to the poloidal transit frequency, this term becomes important. Similarly, transient behavior for which axisymmetric compression of a complete flux tube may not be precluded, such as may be hypothesized for certain disruptive instabilities, requires diagnosis of density perturbations in order to determine the underlying plasma displacement [20]. Again, 2D imaging is essential for arriving at unambiguous solutions.

Finally, imaging both density and temperature fluctuation simultaneously and with capabilities analogous to those demonstrated by ECEI is of undisputed value in diagnosing edge regions of tokamak plasmas. As discussed earlier, plasma in this region is optically thin or grey, and reliable and effective methods of interpreting cyclotron emission are yet to be established. Correlation of ECEI data to density perturbations recorded using MIR promises to provide a foundation for this interpretation. The technical advancements outlined here demonstrate that microwave imaging technology has brought fusion plasma diagnostics to the cusp of a new era, where plasma phenomena are visualized without ambiguity and theoretical models are held to the high standards of readily available experimental observations.

This work supported in part by the U.S. Department of Energy under DE-FG02-99ER54531, SC-G903402, DE-AC02-09CH11466, DE-AC05-00OR22725 and DE-FC02-04ER54698. This work also supported by NWO, POSTECH, and the Association EURATOM-FOM.

[1] T. Munsat *et al.*, Rev. Sci. Instrum. **74**, 1426 (2003).
[2] H. Park *et al.*, Rev. Sci. Instrum. **75**, 3787 (2004).
[3] B. Tobias *et al.*, Rev. Sci. Instrum. **80**, 093502 (2009).
[4] B. Tobias *et al.*, Rev. Sci. Instrum. **81**, 10D928 (2010).
[5] G. S. Yun *et al.*, Rev. Sci. Instrum. **81**, 10D930 (2010).
[6] H. K. Park *et al.*, Phys. Rev. Lett. **96**, 195004 (2006).
[7] H. K. Park *et al.*, Phys. Rev. Lett. **96**, 195003 (2006).
[8] H. K. Park *et al.*, in 23rd IAEA Fusion Energy Conference (Nuclear Fusion, Daejon, Korea Rep. of, 2010).
[9] I. G. J. Classen *et al.*, Rev. Sci. Instrum. **81**, 10D929 (2010).
[10] B. Tobias *et al.*, Phys. Rev. Lett. **106**, 075003 (2011).
[11] E. Mazzucato *et al.*, Phys. Plasmas **9**, 1955 (2002).
[12] H. K. Park *et al.*, Rev. Sci. Instrum. **81**, 10D933 (2010).
[13] E. J. Valeo, G. J. Kramer and R. Nazikian, Plasma Phys. Control. Fusion **44**, L1 (2002).

[14] B. Tobias *et al.*, Contributions to Plasma Phys. **51**, 2-3, 111 (2011).
[15] L. Lei *et al.*, Rev. Sci. Instrum. **81**, 10D904 (2010).
[16] T. Munsat *et al.*, Appl. Optics **49**, E20 (2010).
[17] X. Kong, C. W. Domier and J. N. C. Luhmann, Rev. Sci. Instrum. **81**, 10D923 (2010).
[18] P. Zhang *et al.*, Rev. Sci. Instrum. **79**, 10F103 (2008).
[19] C. W. Domier *et al.*, Rev. Sci. Instrum. **77**, 10E924 (2006).
[20] B. Tobias *et al.*, Phys. Plasmas **18**, 056107 (2011).
[21] C. Z. Cheng and M. S. Chance, J. Comput. Phys. **71**, 124 (1987).
[22] D. A. Spong, B. A. Carreras and C. L. Hedrick, Phys. Fluids B-Plasma **4**, 3316 (1992).
[23] P. H. Diamond *et al.*, Plasma Phys. Control. Fusion **47**, R35 (2005).
[24] A. Kramer-Flecken *et al.*, Phys. Rev. Lett. **97**, 045006 (2006).
[25] S. Yamaguchi *et al.*, Rev. Sci. Instrum. **79**, 10F111 (2008).
[26] T. Yoshinaga *et al.*, Rev. Sci. Instrum. **81**, 10D915 (2010).
[27] D. Kuwahara *et al.*, Rev. Sci. Instrum. **81**, 10D919 (2010).
[28] R. Nazikian, G. J. Kramer and E. Valeo, Phys. Plasmas **8**, 1840 (2001).
[29] G. J. Kramer, R. Nazikian and E. J. Valeo, Plasma Phys. Control. Fusion **46**, 695 (2004).
[30] T. Munsat *et al.*, Plasma Phys. Control. Fusion **45**, 469 (2003).
[31] W. Lee *et al.*, Plasma Fusion Res. **6**, 2402037 (2011).
[32] A. J. Wootton *et al.*, Plasma Phys. Control. Fusion **30**, 1479 (1988).
[33] A. E. White *et al.*, Phys. Plasmas **15**, 056116 (2008).
[34] A. E. White *et al.*, Phys. Plasmas **17**, 020701 (2010).
[35] G. McKee *et al.*, Rev. Sci. Instrum. **70**, 2179 (1999).
[36] A. E. White *et al.*, Rev. Sci. Instrum. **79**, 103505 (2008).
[37] F. F. Chen, Introduction to plasma physics and controlled fusion (Plenum Press, New York, 1984), p. v. <1>.